RESEARCH ARTICLE

NANO · MICRO small
www.small-journal.com

Liquid Metal Doping Induced Asymmetry in Two-Dimensional Metal Oxides

Mohammad B. Ghasemian, Ali Zavabeti, Francois-Marie Allioux, Pankaj Sharma, Maedehsadat Mousavi, Md. Arifur Rahim, Rasoul Khayyam Nekouei, Jianbo Tang, Andrew J. Christofferson, Nastaran Meftahi, Somayeh Rafiezadeh, Soshan Cheong, Pramod Koshy, Richard D. Tilley, Chris F. McConville, Salvy P. Russo, Cuong Ton-That, Jan Seidel,* and Kourosh Kalantar-Zadeh**

The emergence of ferroelectricity in two-dimensional (2D) metal oxides is a topic of significant technological interest; however, many 2D metal oxides lack intrinsic ferroelectric properties. Therefore, introducing asymmetry provides access to a broader range of 2D materials within the ferroelectric family. Here, the generation of asymmetry in 2D SnO by doping the material with $Hf_{0.5}Zr_{0.5}O_2$ (HZO) is demonstrated. A liquid metal process as a doping strategy for the preparation of 2D HZO-doped SnO with robust ferroelectric characteristics is implemented. This technology takes advantage of the selective interface enrichment of molten Sn with HZO crystallites. Molecular dynamics simulations indicate a strong tendency of Hf and Zr atoms to migrate toward the surface of liquid metal and embed themselves within the growing oxide layer in the form of HZO. Thus, the liquid metal-based harvesting/doping technique is a feasible approach devised for producing novel 2D metal oxides with induced ferroelectric properties, represents a significant development for the prospects of random-access memories.

1. Introduction

The recent discovery of polarization and ferroelectricity in two-dimensional (2D) nanomaterials and structures has significant implications for addressing various challenges in the development of next-generation electronic technologies.[1,2] Creating miniature devices with robust ferroelectricity is a continuous challenge since the associated depolarization fields are size dependent, leading to severe reduction of intrinsic polarization and ferroelectricity at low dimensions in the majority of materials.[3]

Tin oxide (SnO) thin layers can be considered an excellent material for electronics and electronic devices. Compared to many other semiconductors, 2D SnO offer great stability under ambient conditions and additionally, Sn is an extremely low-cost metal.

M. B. Ghasemian, F.-M. Allioux, M. A. Rahim, K. Kalantar-Zadeh
School of Chemical and Biomolecular Engineering
University of Sydney
Sydney, NSW 2006, Australia
E-mail: m.ghasemian@sydney.edu.au; k.kalantar-zadeh@unsw.edu.au

M. B. Ghasemian, F.-M. Allioux, M. Mousavi, M. A. Rahim, J. Tang, K. Kalantar-Zadeh
School of Chemical Engineering
University of New South Wales (UNSW)
Sydney, NSW 2052, Australia

A. Zavabeti
Department of Chemical Engineering
The University of Melbourne
Parkville, VIC 3010, Australia

A. Zavabeti, A. J. Christofferson, C. F. McConville
School of Science
RMIT University
Melbourne, VIC 3000, Australia

P. Sharma, J. Seidel
ARC Center of Excellence in Future Low-Energy Electronics Technologies (FLEET)
University of New South Wales (UNSW)
Sydney, NSW 2052, Australia
E-mail: jan.seidel@unsw.edu.au

P. Sharma
College of Science and Engineering
Flinders University
Bedford Park, Adelaide, SA 5042, Australia

P. Sharma
Flinders Institute for Nanoscale Science and Technology
Flinders University
Adelaide, SA 5042, Australia

R. Khayyam Nekouei, P. Koshy, J. Seidel
School of Materials Science and Engineering
University of New South Wales (UNSW)
Sydney, NSW 2052, Australia

A. J. Christofferson, N. Meftahi, S. P. Russo
ARC Center of Excellence in Exciton Science
School of Science
RMIT University
Melbourne, Victoria 3000, Australia

The ORCID identification number(s) for the author(s) of this article can be found under https://doi.org/10.1002/smll.202309924

DOI: 10.1002/smll.202309924

This oxide is known as a viable material for the fabrication of thin-film field-effect transistors (FET) and complementary metal oxide semiconductor (CMOS) devices, and is also used as a channel material in ferroelectric field-effect memories.[4,5] Additionally, owing to its large bandgap (≈4.2 eV), 2D SnO can be exploited as a highly transparent single-layer semiconductor.[6] Although SnO is known to be a p-type material, it can be also made n-type under certain conditions or by doping,[7,8] which makes it a suitable choice for the development of CMOS chips.[9] However, SnO does not show ferroelectric properties. Out of 32 crystal classes, 21 are non-centrosymmetric.[10] Thin SnO has a litharge tetragonal unit cell with a space group of P4/nmm,[7] which falls under the centrosymmetric category and consequently is not piezo- or ferroelectric.

Here we hypothesize that the inclusion of $Hf_{1-x}Zr_xO_2$ in 2D metal oxides will generate ferroelectricity by inducing the necessary crystalline asymmetry. The emergence of ferroelectricity that appears within nanoscale thin layers of HfO_2-based materials and their binary systems with ZrO_2 has been of significant importance for electronics.[11–13] This type of ferroelectricity, which increases with reduced dimensions, indicated that 2D HZO layers will be excellent ferroelectrics for incorporation in capacitors, non-volatile memories, and logic devices, especially in CMOS electronics.[14] Both bulk phases of HfO_2 and ZrO_2 have various polymorphs depending on their synthesis conditions (e.g., pressure and temperature).[15] All of the stable HfO_2 polymorphs possess inversion symmetry, and consequently are not ferroelectric. There are, however, several metastable orthorhombic, fluorite-structured, and polar phases, especially orthorhombic phase space group $Pca2_1$ (oIII phase) which can be stabilized under particular chemical and stress conditions.[16] The formation of the polar oIII-phase has been suggested to be the origin of ferroelectricity in HZO thin layers, which otherwise should be paraelectric.[17] In addition to symmetry elements, other factors including dopants, thickness, grain size, oxygen vacancies, and annealing conditions influence the appearance of ferroelectricity in HfO_2-based thin films.[18] For instance, ferroelectricity can be induced in HfO_2 by doping various elements including Al, Gd, La, Si, Sr, Y, and Zr.[19–21] Appropriate doping of HfO_2 stabilizes the orthorhombic phase by altering the internal stress state and surface energy which facilitates the formation of the oIII phase.[16]

In this work, we demonstrate that doping 2D SnO with HZO induces asymmetry to this material. Applying an efficient method for the inclusion of ferroelectric HZO in SnO layers is a challenge and the incorporation of controlled doping values of Hf and Zr in 2D SnO is yet to be shown with vapor-phase or vacuum-based methods. The conventional synthesis method cannot be easily attempted due to the high melting point of Hf and Zr (2227 and 1852 °C, respectively). To circumvent the temperature challenge, we have developed an alloying strategy using Sn melt to bring down the melting point of accessible Hf and Zr for the deposition of SnO doped with Hf and Zr. Liquid metal approach has been considered to produce different 2D materials of different doping levels, such as Bi_2S_3 and In_2S_3 doped SnS and Bi_2O_3-doped SnO.[7,22] Here, we utilize the low melting point Sn as a metallic solvent to form the desired alloy of Sn-Hf-Zr. The liquid metal-based synthesis takes advantage of the selective enrichment of elements at the interface that can be used as a natural doping methodology for the exfoliation of doped 2D materials from the surface of liquid metals.[7,23–25] Moreover, this strategy mitigates the complexity of the doping process and the need for high-grade cleanroom facilities, at the same time a high degree of control over the outcomes with desired elemental stoichiometry is achievable. Subsequently, using the liquid metal-based process, we harvested large HZO-doped SnO (SnO-HZO) nanosheets. These 2D SnO-HZO layers exhibited a robust ferroelectric performance, larger or comparable with other 2D ferroelectric materials.

2. Results and Discussion

The preparation of the ultrathin sheets is illustrated schematically in **Figure 1a**. The synthesis process consists of a van der Waals exfoliation applied to Sn-Hf-Zr liquid metals followed by printing onto a SiO_2/Si substrate. Non-eutectic Sn-Hf-Zr alloys with different atomic percentages (at%), including $Sn_{0.98}Hf_{0.01}Zr_{0.01}$, $Sn_{0.99}Hf_{0.005}Zr_{0.005}$, and $Sn_{0.998}Hf_{0.001}Zr_{0.001}$ were utilized to understand the effect of various bulk concentrations on the liquid metal surface enrichment. The ratios were chosen based on the maximum solubility of Hf and Zr in Sn at 500 °C, as shown in the estimated ternary phase diagram of Sn-Hf-Zr in Figure S1 (Supporting Information). Even at such small amounts of Zn and Hf, the competition between the solutes and solvents results in the presence of HZO together with SnO as components of the oxide skin. The scanning electron microscopy (SEM) image and energy-dispersive X-ray spectroscopy (EDS) elemental mapping in Figure S2 (Supporting Information) confirm the uniform distribution of elements throughout the $Sn_{0.98}Hf_{0.01}Zr_{0.01}$ alloy. The optical microscopy image in Figure 1b and SEM image in Figure S3 (Supporting Information) revealed a large and uniform 2D layer with lateral dimensions of hundreds of microns after the touch printing of oxide skin from this alloy onto a SiO_2/Si substrate. SEM-EDS mapping was also carried out on large SnO-HZO sheets, harvested from $Sn_{0.98}Hf_{0.01}Zr_{0.01}$ alloy, to explore the homogeneous distribution of elements in nanosheets. As shown in Figure S4 in Supporting Information, sheets are uniformly composed of Sn, Hf, and Zr elements, except the thicker spots where Sn

S. Rafiezadeh, C. Ton-That
School of Mathematical and Physical Sciences
University of Technology Sydney
Ultimo, NSW 2007, Australia
S. Cheong, R. D. Tilley
Mark Wainwright Analytical Centre
Electron Microscope Unit
University of New South Wales (UNSW)
Sydney, NSW 2052, Australia
R. D. Tilley
School of Chemistry and Australian Centre for NanoMedicine
University of New South Wales (UNSW)
Sydney, NSW 2052, Australia
C. F. McConville
Institute for Frontier Materials
Deakin University
Geelong, Victoria 3216, Australia

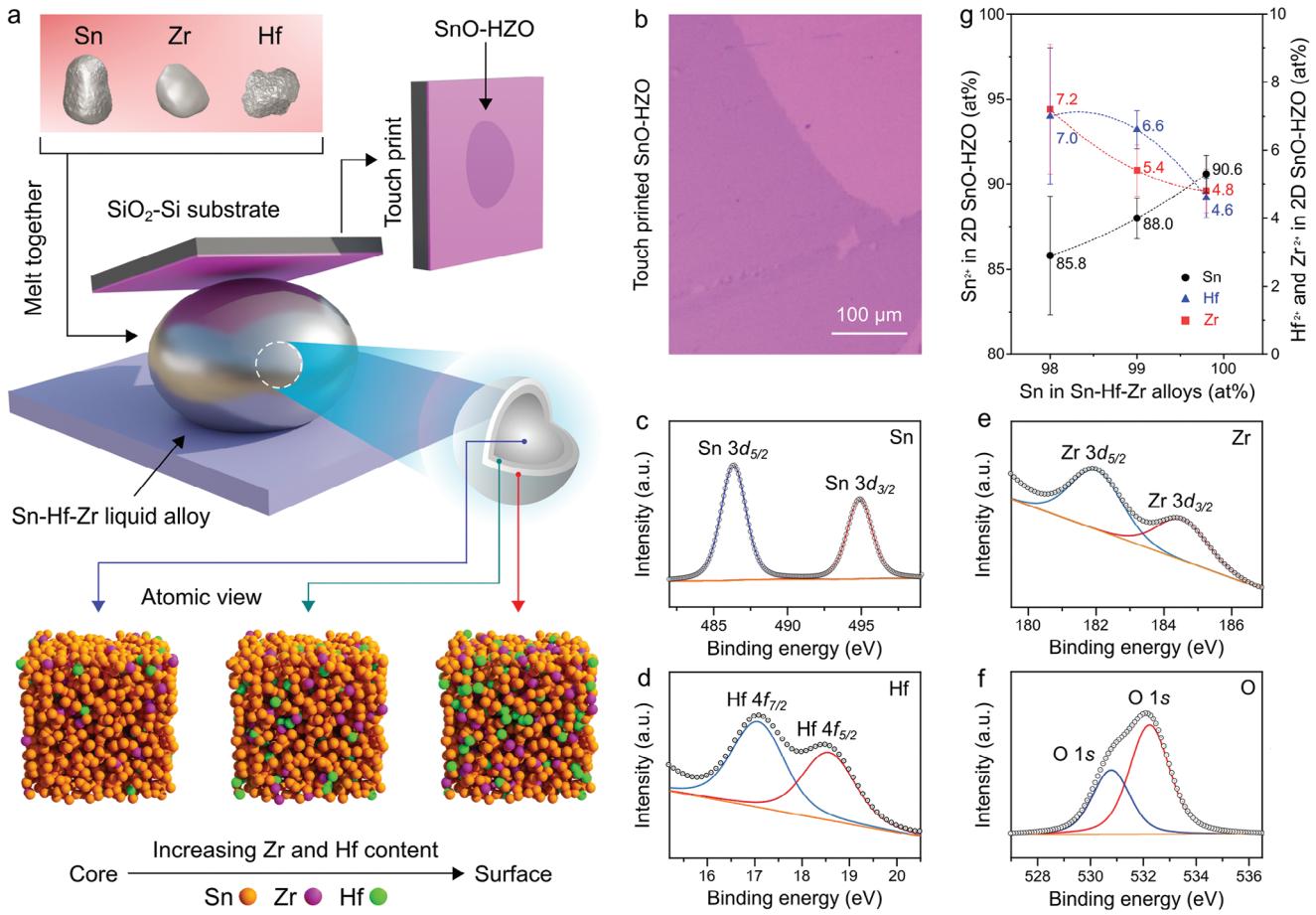

Figure 1. a) Schematic illustration of van der Waals touch printing of SnO-HZO nanosheets from a bulk Sn-Hf-Zr alloy onto a SiO_2/Si substrate through the liquid metal process. b) Optical image of 2D SnO-HZO on the SiO_2/Si substrate showing the large and smooth surface. c–f) XPS spectra of Sn^{2+} ($Sn3d_{3/2}$ and $Sn3d_{5/2}$), Hf^{4+} ($Hf4f_{5/2}$ and $Hf4f_{7/2}$), Zr^{4+} ($Zr3d_{3/2}$ and $Zr3d_{5/2}$), and O^{2-} (O1s), respectively. g) Sn^{2+}, Hf^{4+}, and Zr^{4+} concentrations in the oxide layer measured by XPS versus their initial compositions in Sn-Hf-Zr alloys. Points and error bars represent the average at% of elements and standard errors, respectively, determined from six different samples.

intensity is significantly higher as the representative of bulk value. Even at very low ambient oxygen levels, an atomically thin oxide layer emerges on the surface of the liquid Sn alloy as a result of the interaction between the outermost-surface layer and oxygen through the Cabrera–Mott process.[24] No covalent bonds exist between the non-polar liquid metal and the formed surficial oxide layer. Hence, ultrathin oxide layers can be transferred from the surface of liquid metals to the Si/SiO_2 substrate when the liquid metal and substrate are brought into contact.

The characteristic $Sn3d_{5/2}$ and $Sn3d_{3/2}$ peaks of SnO at binding energies of 486.5 and 495.3 eV, respectively, are shown in the X-ray photoelectron spectroscopy (XPS) spectrum in Figure 1c.[6,7] In the spectrum of Hf (Figure 1d), two peaks appear at 17.0 and 18.5 eV respectively corresponding to the $Hf4f_{7/2}$ and $Hf4f_{5/2}$ orbitals of HfO_2.[26]

Two peaks also were detected for Zr centered at 182.0 and 184.5 eV (Figure 1e) which are respectively attributed to $Zr3d_{5/2}$ and $Zr3d_{3/2}$ orbitals of ZrO_2.[26] The XPS spectrum of O in Figure 1f showed a broad peak which was deconvoluted into two major O1*s* peaks. The peak located at 531.0 eV can be attributed to the lattice oxygen of SnO and HZO, while the sharper oxygen peak at 532.2 eV is either related to the SiO_2 substrate[7] or non-lattice oxygen in SnO-HZO,[27] or a combination of both.

The atomic percentages of elements in the touch-printed interfacial oxide nanosheets harvested from $Sn_{0.98}Hf_{0.01}Zr_{0.01}$, $Sn_{0.99}Hf_{0.005}Zr_{0.005}$, and $Sn_{0.998}Hf_{0.001}Zr_{0.001}$ liquid alloys are determined by quantitative XPS and listed in **Table 1**. Importantly, as shown in Figure 1g, the atomic concentrations of Sn, Hf, and Zr in the nanosheets are significantly different from their contents in the bulk liquid metal. In the case of the $Sn_{0.98}Hf_{0.01}Zr_{0.01}$ alloy, the atomic ratios of Hf and Zr equally increased (by a factor of seven each in the 2D sheets) while the Sn content dropped by 14%. This variation is even more prominent for nanosheets obtained from the $Sn_{0.998}Hf_{0.001}Zr_{0.001}$ liquid metal where the atomic ratios of Hf and Zr increased more than forty-five times in nanosheets compared to their original values in liquid metal. Similar phenomena and disproportionate atomic ratios of elements at the surface and the bulk of liquid alloys have been observed for other 2D metal oxides, such as indium tin oxide (ITO) and TeO_2, through the liquid-metal-based synthesis.[7,23,24]

The preferential surface metal oxide sheets formed from the content of liquid metal alloys depend on several critical factors

Table 1. The atomic percentage of Sn, Hf, and Zr elements in Sn-Hf-Zr liquid alloys and their corresponding atomic ratios in the harvested 2D oxide sheets.

	Sn	Hf	Zr	Alloy / Oxide*	Sn	Hf	Zr	Alloy / Oxide*	Sn	Hf	Zr	Alloy / Oxide*
at% in liquid metal	98.0	1.0	1.0	$Sn_{0.98}Hf_{0.01}Zr_{0.01}$	99.0	0.5	0.5	$Sn_{0.99}Hf_{0.005}Zr_{0.005}$	99.8	0.1	0.1	$Sn_{0.998}Hf_{0.001}Zr_{0.001}$
at% in 2D oxide sheets	85.8±3.5	7.0±2.0	7.2±1.9	0.86SnO-0.14HZO	88.0±1.2	6.6±0.6	5.4±0.8	0.88SnO-0.12HZO	90.6±1.1	4.6±0.6	4.8±0.6	0.91SnO-0.9HZO

*The atomic ratios of oxygen in 2D oxide sheets were realized from the XPS analyses.

including their solubility, metallic solvent temperature, and Gibbs free energy of oxidation for the individual elements.[28] The natural filtering mechanism based on different migration tendencies of elements in liquid metals can be feasibly utilized for the controlled preparation of doped 2D sheets with desired atomic ratios through adjusting the atomic ratios of metals in the bulk of liquid metals and monitoring their ratios at the harvested sheets. The Gibbs free energy value for the formation of SnO, HfO_2, and ZrO_2 are −251.9, −1088.2, and −1042.8 kJ mol^{-1} respectively.[29] Thermodynamically, Hf and Zr have a stronger tendency for surface entrapment and oxidation when compared to Sn, as explained by the lower Gibbs free energies relative to Sn. Consequently, oxygen in the vicinity of the interfacial layer interacts at a greater rate with Hf and Zr despite their lower concentrations in the bulk. The close Gibbs free energy values and almost equal atomic/ionic radii of Hf and Zr govern their near-equal ratio migrations to the interface. The XPS depth profile (Figure S5, Supporting Information) on micron-sized Sn-Hf-Zr droplets shows continuous decrease in the Sn^{2+}/Sn^0 intensity ratio with increasing etching time confirming the formation of the oxide layer on the droplet surface. Here, HZO-doped SnO or SnO-HZO follows the definition of (1-x)SnO-(x)HZO for which 0<x<1. From the qualitative and quantitative XPS studies, and Table 1, it is concluded that the oxide nanosheets harvested from the surface of the liquid Sn-Hf-Zr alloys possess chemical compositions corresponding to 0.86SnO-0.14HZO, 0.88SnO-0.12HZO, and 0.91SnO-0.9HZO. Since it is assumed that HZO induces ferroelectricity in the 2D SnO, the harvested nanosheet with the highest ratio of HZO (0.86SnO-0.14HZO) is the preferred specimen and was used for the next studies and characterization analysis.

As shown in **Figure** 2a, in the bulk, there were no persistent Zr-Zr, Hf-Hf, or Zr-Hf direct contacts, but the Zr and Hf separation remained consistently at ≈6 Å from each other, separated by a Sn atom, with Sn-Sn, Sn-Zr, and Sn-Hf direct contacts at ≈3 Å, which is the configuration that provides a thermodynamically stable equilibrium. This suggests that in bulk Zr and Hf remain associated, but not aggregated. At the interface, direct Zr-Zr, Hf-Hf, and Zr-Hf contacts were observed, at 3.5, 3.3, and 3.4 Å, respectively (Figure 2b). In this case, Zr and Hf were found to be distributed similarly throughout the system at a depth up to one atomic layer below the interface but were completely excluded from the interfacial layer itself. (Figure 2c).

To examine the structure and dynamics of the initial oxide formation, six O_2 molecules were added above the interface. The MD process is explained in Note 1 (Supporting Information). As shown in Figure 2d, some of the O_2 reacted rapidly with the surface Sn to form SnO clusters, and others diffused several atomic layers below the interface to interact with Zr and Hf, with Sn-O contacts at ≈2.2 Å and Zr-O and Hf-O contacts at ≈2 Å. Over time, the SnO clusters tended to protrude from the interface, while the HZO clusters were found either at or below the interfacial layer, but not directly below the SnO clusters (Figure 2e). The motion in this direction is dictated by the forces of atoms as this configuration minimizes the total energy of the system. Likewise, based on the forces and energies, as the liquid Sn becomes solid SnO, it is more energetically favorable for SnO to be found above the liquid Sn rather than above the HZO clusters. This spatial separation

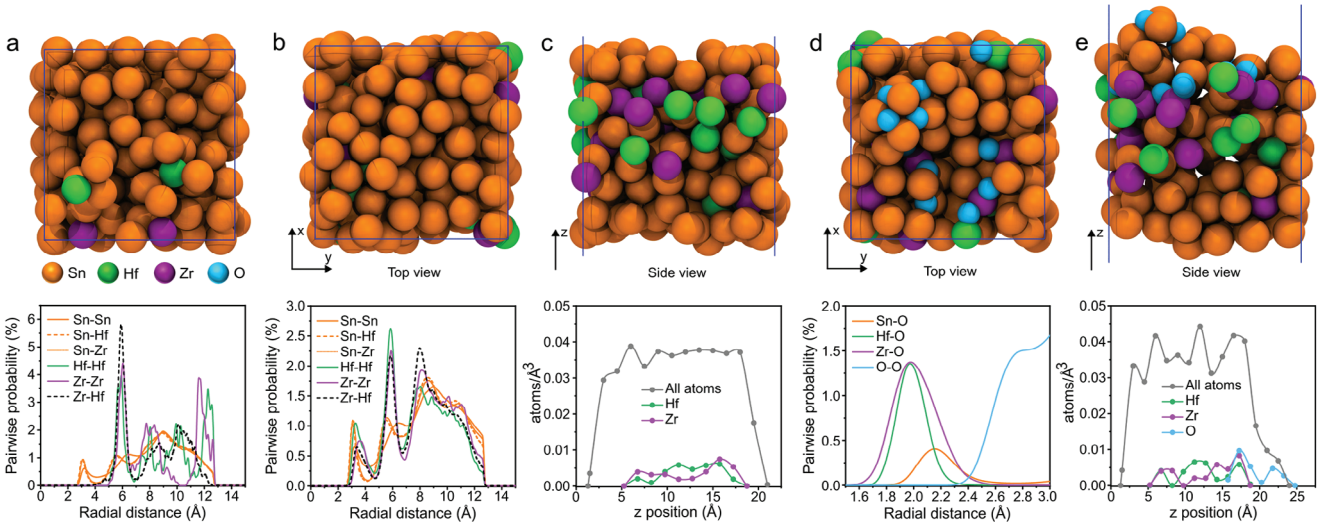

Figure 2. a) Snapshot of bulk 196 Sn 2Hf 2Zr system and atomic pairwise probability distribution in the bulk. b) Snapshot top view of the interfacial system comprising 170 Sn 15 Hf 15 Zr, and atomic pairwise probability distribution at the interface. c) Snapshot cross-section view of the interfacial system comprising 170 Sn 15 Hf 15 Zr, and atomic density profiles as a function of *z* position at the interface. d) Snapshot top view of the interfacial system comprising 170 Sn 15 Hf 15 Zr 12 O, and atomic pairwise probability distribution of O interactions at the interface. e) Snapshot cross-section view of the interfacial system comprising 170 Sn 15 Hf 15 Zr 12 O, and atomic density profiles as a function of *z* position at the interface.

provides a potential explanation for how SnO and HZO oxides could simultaneously form adjacently as the system is cooled.

The Raman spectrum in Figure S6 (Supporting Information) shows the corresponding modes of SnO and HZO in the harvested SnO-HZO nanosheets (see the assignment of Raman peaks in Note 2, Supporting Information). The weak intensity of the HZO Raman peaks compared to SnO peaks indicates the small portion of HZO in 2D SnO-HZO as determined by quantitative XPS measurements. The XRD pattern of the SnO-HZO nanosheets is shown in **Figure 3a** and is further discussed in Supplementary Note 3 in Supporting Information. The XRD pattern of the bulk Sn-Hf-Zr alloy with a thick oxide shell is also presented at the bottom of the figure (as a reference). Peaks located at 28.4° and 32.1° are attributed to the (011) and (110) planes of SnO, respectively.[6,7] The XRD peaks at 30.7°, 34.7°, and 43.4° are assigned to the (111), (020), and (112) characteristic planes of orthorhombic HZO, respectively.[5,12] The intensity of oxide to metallic peaks increased significantly in the XRD pattern of SnO-HZO nanosheets indicating that the composition of the nanosheets is dominated by SnO and HZO.

The EDS observation (Figure 3b) through transmission electron microscope (TEM) revealed the uniform distribution of Sn, Hf, Zr, and O in the entire nanosheet, with a higher Sn intensity. The bright-field TEM image in Figure 3c shows mostly smooth layers with some wrinkles and a translucent appearance indicating the ultrathin nature of nanosheets. The high-resolution TEM (HRTEM) images (Figure 3d) revealed the presence of both SnO and HZO phases in harvested nanosheets from the surface of the Sn-Hf-Zr alloy, which is further discussed in Supplementary Note 4 (Supporting Information).

The nanosheets possess polycrystalline nanograins of SnO and HZO distributed in random orientations. The selected area electron diffraction (SAED) pattern of the nanosheets with the coexistence of SnO and HZO phases and their corresponding lattice spacings and planes are shown in Figure 3e. The HRTEM image and SAED pattern of 2D SnO-HZO point to the lattice spacings of 0.27 and 0.31 nm matching (1-10) and (011) planes of tetragonal SnO, respectively, while the 0.29 nm belongs to (111) plane of orthorhombic HZO. Figure 3f shows the HRTEM image of a nanograin that projection matched that of a tetragonal SnO viewed down a <111> zone axis. Nanograin with an orientation matching that of a <111> projection of orthorhombic HZO, with noticeable lattice distortion as indicated by the diffuse reflections on the fast Fourier transform (FFT) pattern, was also observed, as shown in Figure 3g (see Note 4 and simulated pattern in Figure S7, Supporting Information).

Kelvin probe force microscopy (KPFM), electron energy loss spectroscopy (EELS), XPS valence band, and cathodoluminescence (CL) measurements were carried out on 2D SnO-HZO to establish its electronic band structure. The surface morphology and layer thickness of the nanosheets were also revealed during the atomic force microscopy (AFM) and KPFM assessment. For these measurements, 2D ITO nanosheet were deposited on SiO_2/Si substrate, also using a liquid metal process[24] (XRD pattern in Figure S8, Supporting Information).

As shown in **Figure 4a**, overall, the nanosheets possess smooth and uniform surfaces. A step height of 0.5 nm was observed between 2D SnO-HZO and ITO nanosheets, is in excellent agreement with the interplanar spacing of SnO crystals (0.48 nm),[6] indicating the ultrathin and monolayer nature of the 2D SnO-HZO. The contact potential difference (CPD) was captured between the KPFM tip (Pt/Ir coated tip) and SiO_2/Si substrate, SnO-HZO, and ITO nanosheets. The CPD is defined as $\Phi_{tip}-\Phi_{sample}$. As shown in Figure 4b, contact potential differences of 80, 277, and 247 mV were obtained for SiO_2/Si, ITO, and SnO-HZO against the tip. The work function of the tip was determined to be 4.69 eV.[30] Therefore, the work functions of ITO and SnO-HZO nanosheets can be calculated as 4.41 and 4.44 eV, respectively.

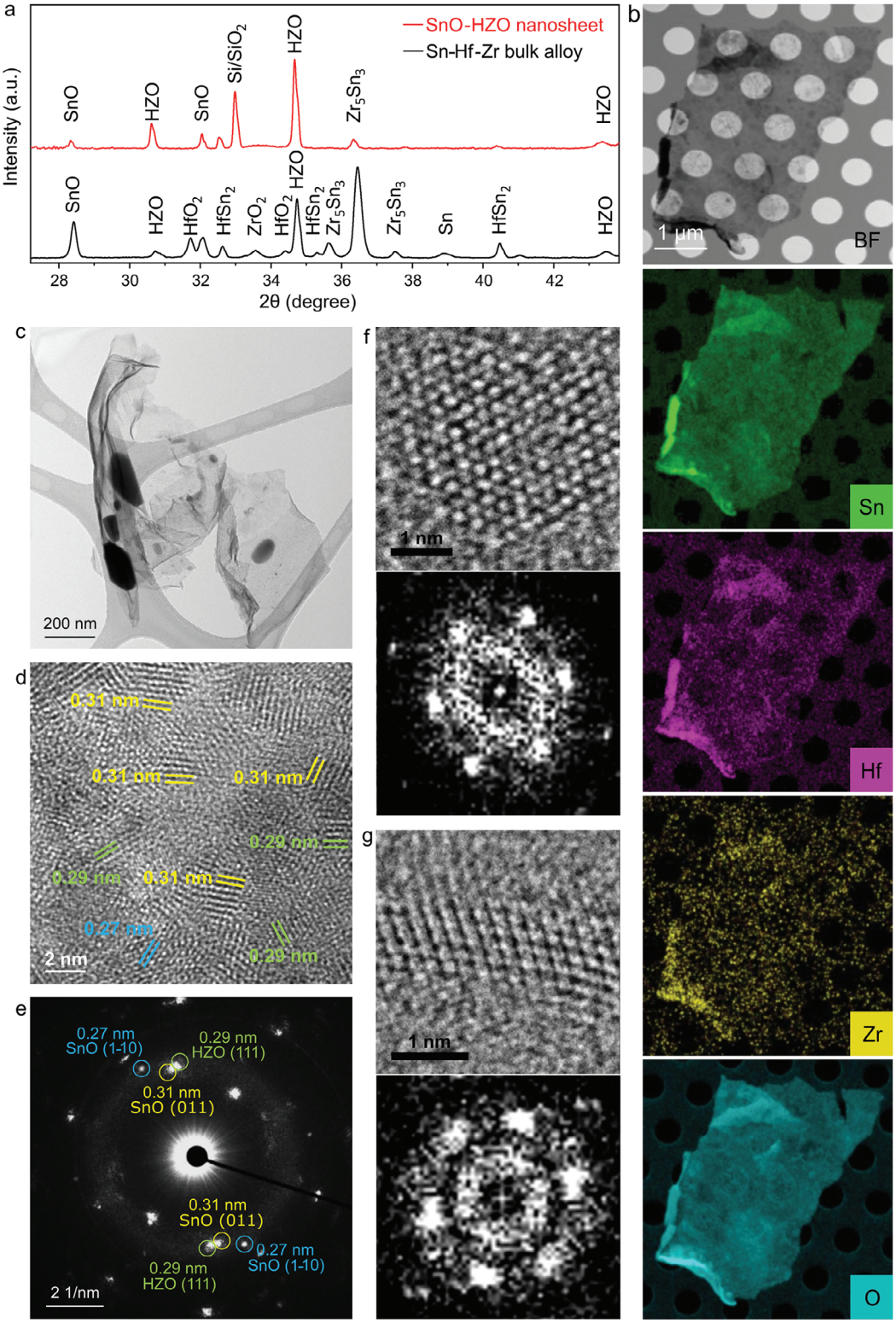

Figure 3. a) XRD pattern of SnO-HZO nanosheets (top) harvested by multiple exfoliations from the surface of bulk Sn-Hf-Zr alloy (bottom) in liquid form. The XRD pattern for the bulk alloy mostly exhibits metallic peaks which are absent in nanosheets while the intensity of oxide peaks increased. b) EDS elemental mapping of 2D SnO-HZO with uniform distribution of elements throughout the thin nanosheet. The intensity of Sn is significantly higher than Hf and Zr. The analysis of EDS mappings shows an atomic ratio of 81% for Sn to Hf and Zr in SnO-HZO nanosheets, as closely confirmed by XPS quantitative measurements. c–e) Bright-field TEM, HRTEM, and SAED pattern of 2D SnO-HZO, respectively., indicating the coexistence of SnO and ferroelectric HZO in the harvested nanosheets. f,g) HRTEM images and their corresponding FFT patterns of SnO and HZO nanograins, respectively.

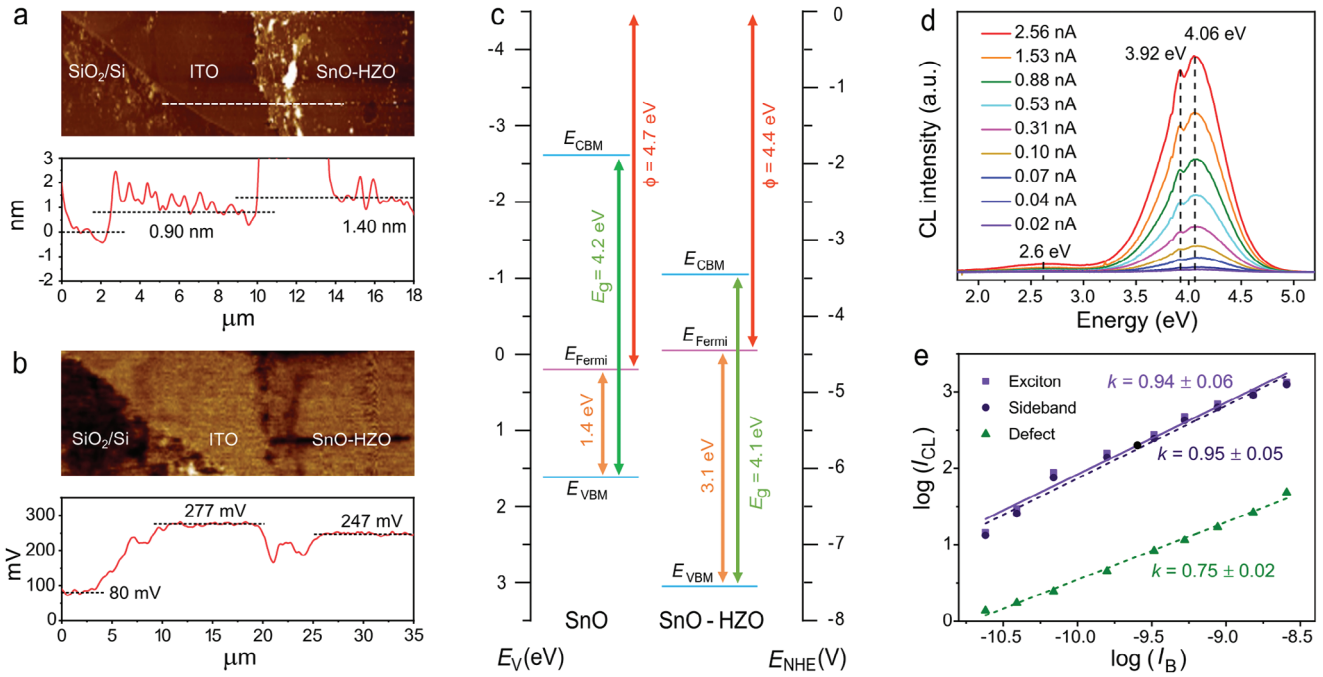

Figure 4. a) The AFM image and height profile along the dashed line. Some thicker parts of the nanosheet can be seen occasionally along the edges due to the restacking of nanosheets during the touch printing process. b) KPFM measurements of SnO-HZO nanosheets with underlayer ITO nanosheets on a SiO_2/Si substrate, showing thicknesses of ≈0.9 and ≈0.5 nm, and work functions of 4.41 and 4.44 eV for ITO and SnO-HZO nanosheets, respectively. c) The band diagram of SnO-HZO nanosheets structured using KPFM, EELS, and XPS information. The band diagram of SnO is also shown as a reference to reveal the effect of HZO incorporation. d) CL spectra at 80 K for the SnO-HZO nanosheets collected with various e-beam currents, showing excitonic, sideband, and defect-related emission peaks. The peak positions and spectral lineshape are unchanged as the probing area and e-beam current are increased, indicating the uniformity of crystallinity and defect distribution across the nanosheet. e) Plot of $\log(I_{CL})$ versus $\log(I_B)$ at 80 K with I_B in nA. Power-law fits by straight lines show an almost linear relationship with excitation power for the excitonic and sideband emissions with $k = 0.95$, whereas the defect-related emission displays sub-linear dependency with excitation power due to the saturation of defect states.

The measured work function for ITO is a close match to past literature,[31] and implying that the estimated work function for 2D SnO-HZO to be accurate.

A bandgap (E_g) of 4.10 eV was determined for the nanosheets by extrapolating the linear fits of the electron loss energy to loss intensity, as shown in the enlarged EELS spectrum Figure S9 (Supporting Information). As shown in Figure S10 (Supporting Information), 2D SnO-HZO, which is predominantly composed of SnO, showed an excellent fit ($R^2 > 0.99$) to the indirect bandgap. Using the same methods, an indirect bandgap of 4.20 eV has also been reported for SnO monolayers.[7] The position of valence band maximum (VBM) and conduction band minimum (CBM) were estimated at −7.54 eV and −3.44 eV, respectively, using the XPS valence band spectrum (Figure S11, Supporting Information) and discussion in Note 5 (Supporting Information). The electronic band structure of the 2D SnO-HZO was plotted and compared with the previously reported SnO nanosheets in Figure 4c. This band diagram provides important information about the distribution of energy levels in nanosheets and the nature of nanosheets before and after doping which is crucial for the better understanding of the optical and electronic properties of nanosheets when designing electronic devices. Additionally, the band diagram reasserts the successful doping of SnO with HZO as well as the significant role of HZO in the modulation of the band structure and optical properties of SnO. The measured work function for SnO-HZO nanosheets (4.44 eV) is larger than that of HZO (3.86 e V),[32] and closer to that of SnO (4.70 eV).[7] Here, the SnO-HZO nanosheet also possessed a slightly smaller bandgap of 4.10 eV, compared to its SnO counterpart which has an indirect bandgap of 4.20 eV. In addition, 2D SnO-HZO exhibited clear n-type behavior since the Fermi level has moved closer to the conduction band-edge after the incorporation of HZO in p-type SnO. This shift can be attributed to the narrowing of the bandgap (from 4.2 to 4.1 eV) due to different interaction effects among free charge carriers or between free carriers and ionized impurities.[33] Additionally, based on the well-known Burstein–Moss effect,[34] the Fermi level can move higher toward the conduction band due to the increase in carriers' concentration after doping.

The CL spectra of individual SnO-HZO nanosheets, shown in Figure 4d, reveal three emission peaks: an excitonic emission at 4.06 eV, a side-band peak at 3.92 eV, and a broad defect-related emission at ≈2.6 eV. The excitonic emission energy observed at 4.06 eV is entirely consistent with the measured bandgap of 4.1 eV determined by EELS. The nature of the 3.92 eV peak is unknown at this stage, but its sharp peak suggests this emission is related to bound excitons in the 2D nanosheet. The defect emission at ≈2.6 eV in SnO nanosheets has previously been attributed to Sn vacancies.[35] Normalized CL spectra are shown in Figure S12 (Supporting Information) suggesting that the luminescence emission is uniform across the nanosheet. The recombination kinetics of the three emission bands are illustrated in

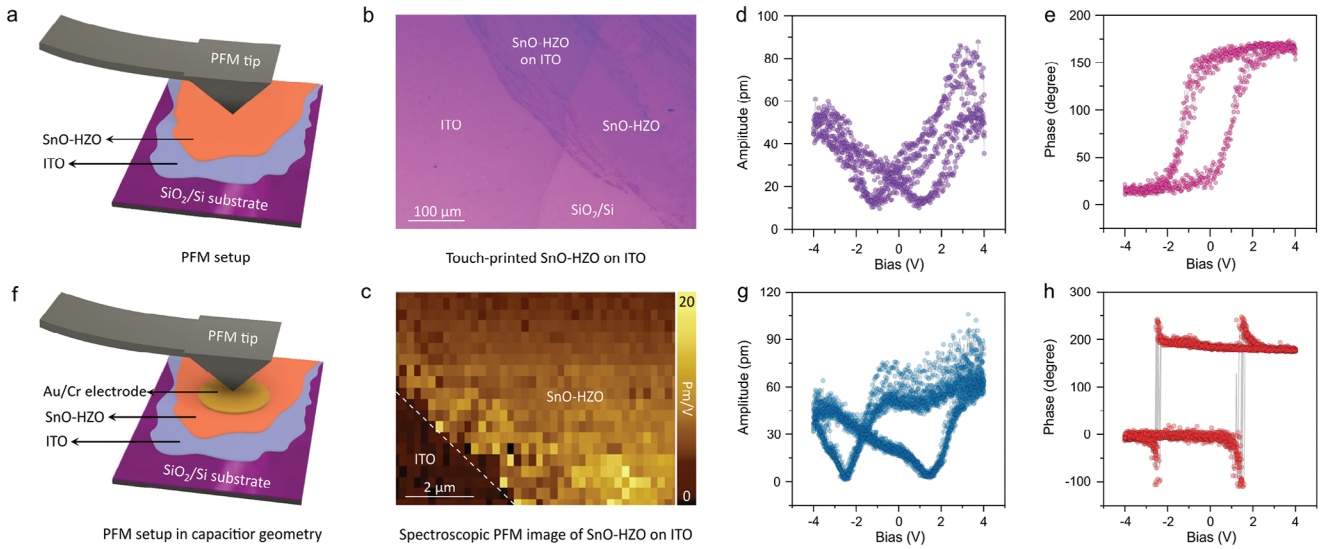

Figure 5. a) Schematic illustration for PFM measurements. b) optical microscopy image of a SnO-HZO nanosheet with an underlying conductive ITO nanosheet deposited on a SiO_2/Si substrate for ferroelectricity measurements. SnO-HZO and ITO nanosheets were deposited on the substrate through the liquid metal process. c) PFM spectroscopic measurements on the edge of a SnO-HZO and ITO nanosheets showing the switchable hysteresis response and ferroelectricity for SnO-HZO nanosheets compared to ITO. d,e) typical PFM amplitude butterfly and phase hysteresis loops, respectively, confirming the ferroelectric properties of SnO-HZO nanosheets with a d_{33} of ≈10 pm V^{-1}. f) Schematic illustration for the PFM measurements of SnO-HZO nanosheets with underlying ITO nanosheets in a capacitor geometry. g,h) spectroscopic PFM amplitude butterfly and phase hysteresis responses of SnO-HZO nanosheets obtained through the top metal electrodes confirming switchable hysteretic polarization and ferroelectric characteristics.

the log-log plot in Figure 4e, and are further discussed in Note 6 (Supporting Information). The power law fits yield the exponent $k = 0.94 \pm 0.06$, 0.95 ± 0.05, and 0.75 ± 0.02 for the excitonic, sideband, and defect-related emissions, respectively. The excitonic and sideband emissions show an identical, linear relationship with excitation power with k ≈1 because the recombination rate of free and bound excitons is smaller than the carrier injection rate by the electron beam.[36] On the other hand, the defect emission at 2.6 eV displays a sub-linear relationship with excitation power due to the saturation of defect states. This result also confirms that both 4.06 and 3.92 eV emissions are excitonic in nature and not related to a lattice-coupled defect. Conversely, the defect-related emission displays a strongly sub-linear dependence with excitation power as this luminescence emission originates from a lattice-coupled deep-level defect.

Figure 5a schematically depicts the electrically conductive nanoscale tip and deposited 2D SnO-HZO layers buffered with ITO that serves as the bottom metal contact for the piezoresponse measurements. The 2D SnO-HZO and ITO layers are also seen in the optical microscopy image shown in Figure 5b. An AFM probe with the tip radius much larger than the size of HZO nanograins was used for the ferroelectric measurements. Thereafter, spectroscopic piezoresponse force microscopy (PFM) measurements were performed over this area encompassing the boundary, as shown in Figure 5c. The acquired representative spectroscopic PFM response on the SnO-HZO sheet is displayed in Figure 5d,e, which shows a hysteretic behavior and the presence of two electrically switchable polarization states. The PFM amplitude response displays a characteristic butterfly curve (Figure 5d), while the corresponding phase response displayed a phase change of 180° (phase inversion), at the minima of the amplitude response, indicating the presence of bistable remanent polarization states (Figure 5e).[37] These electrically switchable bistable polarization states provide evidence for the ferroelectricity observed in the SnO-HZO nanosheets. Ferroelectric measurements were carried out on different points of the SnO-HZO nanosheets and rendered same ferroelectric responses, as shown in Figure S13 (Supporting Information), conforming the switchable hysteresis response and homogenous ferroelectricity throughout the SnO-HZO nanosheets. Moreover, a strong piezoelectric response (effective d_{33}) of ≈10 pm V^{-1} was achieved for the nanosheets, estimated from the slope of the linear part of the piezoresponse amplitude–voltage butterfly loop, and was observed only for the SnO-HZO layer. In contrast, as expected, no detectable piezoresponse or switchable behavior was observed beyond the boundary of the ITO layer (Figure 5c; Figure S14, Supporting Information).

In addition, the acquired piezoelectric coefficient for SnO-HZO nanosheets (≈10 pm V^{-1}) was found to be higher than or comparable to that reported for doped ZrO_2 (10 pm V^{-1})[38] and doped HfO_2 (1 pm V^{-1},[39] 3.8 pm V^{-1}[40] and 19.8 pm V^{-1}[41]) and $Hf_{1-x}Zr_xO_2$ thin films (0.25 pm V^{-1}[42], 5.5 pm V^{-1}[39] and 10 pm V^{-1}[43]). The observed ferroelectricity and electrically switchable polarization behaviors are also consistent with the presence of the orthorhombic phase of the HZO.[44]

The PFM measurements could, in principle, be affected by charge injection, surface charging, and other electrostatic effects.[45] To rule out these factors, the spectroscopic PFM measurements were conducted through a metal-gated SnO-HZO layer, i.e., in a capacitor geometry. For this, 55 nm-thick Au/Cr top metal electrodes were deposited on the nanosheets through the lithography process, as shown schematically in Figure 5f. Subsequently, the spectroscopic PFM responses were acquired on nanosheets through the top metal electrodes. In agreement with

previous measurements, clear electrically switchable polarization states, and a hysteretic behavior are observed (Figure 5g,h), indicating the presence of robust ferroelectricity of SnO-HZO nanosheets. To confirm the role of the HZO in the emergence of ferroelectricity in SnO nanosheets, the ferroelectricity measurements were performed on pure SnO nanosheets prepared by the same liquid metal synthesis process. As shown in Figure S15 (Supporting Information), no switchable hysteresis response, amplitude butterfly, and phase hysteresis loops were observed for the pristine SnO without the HZO dopants, clearly indicating the successful induction of ferroelectricity in 2D SnO through the liquid metal-based HZO doping.

The enhancement of ferroelectricity in HZO has been observed when it was thinned down to below 30 nm.[17] This improvement was particularly noticeable when the HZO layer had minimal roughness, fine grains, and sufficient crystallization. The development of the monoclinic phase is restrained in ultrathin HZO due to the higher surface energy associated with smaller grain sizes.[48] It can also promote the formation of the orthorhombic phase, which is advantageous for enhancing the ferroelectric properties, leading to the appearance of ferroelectricity in ultrathin HZO-doped SnO nanosheets.

The generation of ferroelectricity in SnO-HZO nanosheets can be associated to the coexistence and strong interactions between the SnO and HZO phases due to their epitaxial strain. This heterogeneity in the structure would mean that deformation of the material in different regions of nanosheets would vary due to varying strength of coupling to the applied electric field in each of those regions. This variation in deformation could result in higher strain values thus leading to leading d_{33} results. It is not uncommon that small changes in the chemical composition leads to major alterations in the ferroelectric properties of oxide layers. Ferroelectricity has been suggested to form in thin films of SiO_2-doped HfO_2 when an orthorhombic ferroelectric phase with a $Pbc2_1$ space group is formed due to inhibition of the tetragonal to monoclinic transformation by mechanical confinement.[11] Additionally, it has been established that the strain is particularly effective in altering the stable crystal structure of thin films for the generation or enhancement of ferroelectricity. The strain-driven phase changes due to the coexistence of tetragonal and rhombohedral phases are also known as the origin of ferroelectricity in $BiFeO_3$ thin films.[49] The lattice mismatch and generated epitaxial strain between SnO and HZO structures are calculated and illustrated in Note 7 and Figure S16 (Supporting Information) for the successful formation of epitaxial heterostructures leading to the advent of ferroelectricity in SnO-HZO nanosheets.

3. Conclusions

We employed a liquid metal-based doping process to induce asymmetry in the semiconducting SnO nanosheets through the formation of a HZO phase within nanosheets. Regardless of concentration, the dissolved metallic elements migrate from bulk to the surface of liquid metals based on their atomic interactions and dynamics of initial oxidization which leads to natural selective doping of the surface oxide layer. This concept enables the harvesting of nanosheets composed of high melting point elements from the surface of liquid metals at moderate temperatures through a liquid metal contact-print process. Hence, we have used this concept to incorporate ferroelectric HZO into SnO nanosheets. Despite using only extremely small atomic ratios (≤1%) of Hf and Zr in Sn-Hf-Zr liquid metals, these elements transferred more effectively to the interface and formed the HZO phase as the dopant in the harvested SnO nanosheets.

Molecular dynamic simulations provided atomic insights in regard to elemental interactions in the liquid state and the role of spatial separation in evolving the HZO phase in SnO nanosheets. HZO-doped SnO nanosheets exhibited n-type characteristics in contrast to the p-type nature of SnO nanosheets. In addition, the harvested nanosheets demonstrated a strong ferroelectricity of 10 pm V^{-1} confirming successful doping and the presence of orthorhombic ferroelectric HZO in nanosheets. This work suggests an extremely efficient pathway to the generation of ultrathin ferroelectric sheets by introducing ferroelectric phases as the dopant in nanosheets through a liquid metal process.

4. Experimental Section

Alloys Preparation: Tin (Sn, 99.99%, Rotometals), Hafnium (Hf, 99.7% Sigma–Aldrich), and zirconium (Zr, 99.98%, Sigma–Aldrich) were mixed at different atomic ratios and melted together using an induction heater (Across International Induction Heating Machine) in an argon atmosphere to render $Sn_{0.98}Hf_{0.01}Zr_{0.01}$, $Sn_{0.99}Hf_{0.005}Zr_{0.005}$, and $Sn_{0.998}Hf_{0.001}Zr_{0.001}$ alloys. These atomic ratios were selected based on the maximum solubility of Sn with Hf and Zr in temperatures below 500 °C.

Doped Oxide Nanosheet Touch Printing: The exfoliation and touch-print process of SnO-HZO nanosheets were carried out under controlled interfacial oxidation by melting the Sn-Hf-Zr alloys at 500 °C in a nitrogen glovebox (O_2 <0.5 ppm). The reference SnO nanosheets were collected from the surface of liquid Sn at the same exfoliation conditions as SnO-HZO. An atomically thin oxide layer emerges on the surface of Sn-Hf-Zr molten alloy through the self-limiting Cabrera–Mott reaction.[50] There is no covalent bond between the liquid metal and its surface oxide. However, there is a strong van der Waals interaction between the oxide layer on liquid alloy and the transfer substrate (SiO_2/Si). The layer is stabilized on the substrate by the strong van der Waals forces between the surficial oxide layer and permanent dipoles of the substrate.[30]

Therefore, when the Sn-Hf-Zr liquid metal is brought into contact with a SiO_2/Si substrate, an atomically thin layer of metal oxides is transferred from the liquid metal to the substrate. No significant metallic XPS peaks were observed for Sn, Hf, and Zr, indicating the oxide nature of 2D sheets with a uniform SnO, HfO_2, and ZrO_2 composition. ITO nanosheets were transferred through a liquid metal touch print approach from the surface of a liquid In-Sn alloy (95:5 at%, respectively) to a SiO_2/Si substrate at 200 °C and in ambient air. ITO nanosheets were deposited as an underlayer to provide the substrate conductivity as well as a reference for comparison of nanosheets' work functions. The harvested ITO nanosheets have presented a resistance range between 5.4 and 69.6 $k\Omega^{-1}$ depending on the number of layers.[24]

Characterization: The ternary phase diagram of Sn-Hf-Zr alloy was plotted using FactSage 8.1 software – Phase Diagram Module (GTT-Technologies). Surface morphology, EDS mapping, and rough elemental composition for the bulk alloy were observed by a JEOL JSM-IT500HR FE-SEM. The chemical states of Sn, Hf, Zr, and O elements in the harvested sheets were studied by XPS. A Thermo Scientific K-alpha XPS spectrometer with a monochromatic Al Kα source (hv = 1486.6 eV) and a concentric hemispherical electron analyzer (CHA) were used for core-level XPS and valence band analysis on conductive substrates. The pass energy of the analyzer was set to 30 eV for the reported core-level spectra and 100 eV for the wider survey scans (not shown). Samples were blown with N_2 gas before any measurement to remove dust. The XPS measurements were conducted on smooth and clean sheets where there was minimal

presence of metallic inclusion. The presence of HZO in 2D SnO was studied by Raman spectroscopy. The Raman spectrum of the SnO-HZO nanosheets was collected at the range of 110–330 cm^{-1} by Raman spectroscopy (inVia Renishaw) with a laser source of 532 nm. The phase composition of the bulk Sn-Hf-Zr alloy and SnO-HZO nanosheets were studied using Cu Kα radiation ($\lambda = 1.54$ Å) by multi-purpose XRD and Empyrean thin-film XRD instruments, respectively. To enhance the signal for Raman and XRD characterizations, multiple touch print cycles were carried out later to accumulate the number of layers (Figure S17, Supporting Information), which relatively increased the presence of metallic inclusions on nanosheets. TEM was used for in-depth analysis of 2D SnO-HZO touch printed directly on holly silicon nitride grids. Bright-field images, SAED patterns, and elemental mappings of nanosheets were captured using a JEOL F200 HRTEM-EDS system. The SnO-HZO nanosheets were touch printed on TEM grids with lacy carbon or holey silicon nitride support films (Ted Pella, INC.) for HRTEM analysis. GrandARM300F2 equipped with a Gatan K3 direct electron detector for negative spherical aberration corrected TEM imaging.

The thickness, surface topography, contact potential, and the work function of nanosheets were acquired through AFM and KPFM measurements (Bruker Dimension ICON SPM) using a Pt/Ir coated tip. The bandgap of the SnO-HZO nanosheets was measured at 200 kV using a JEOL 2100F EELS and Gatan Tridium imaging filter. The acquired data were fitted into energy equations in a MATLAB curve fitting toolbox to realize the direct/indirect nature of the bandgap. The EELS graph was interpreted by fitting in a non-linear least squares equation solver in the MATLAB optimization toolbox. EELS data were fitted to $\alpha h\nu \propto (h\nu - E_g)^n$ equation, where E_g is the bandgap, $h\nu$ is the photon energy, and α is a constant. Direct and indirect transitions are corresponding to $n = 1/2$ and 3/2, respectively.[51] Transmission-mode CL with spatial resolution < 10 nm was used at 80 K to investigate the optical properties and electronic band structure of SnO-HZO nanosheets. CL characterization of individual nanosheets was conducted in an FEI Quanta 200 SEM equipped with a parabolic mirror and a QE65000 Ocean Optics spectrometer. All luminescence spectra were corrected for the total response of the optical collection system.

Molecular Dynamics (MD) Simulations: AIMD simulations were performed to obtain a better understanding of the behavior of Zr and Hf in the Sn bulk and at the interface, and the initial formation of SnO and HZO oxide clusters at the interface. Initial classical molecular dynamics simulations were carried out on bulk systems comprising 196 Sn atoms, 2 Zr atoms, and 2 Hf atoms, and interfacial systems comprising 170 Sn atoms, 15 Zr atoms, and 15 Hf atoms, in the NVT ensemble at 723.15 K in a 17.931 × 17.931 × 17.931 $Å^3$ box using the MD code LAMMPS.[52] Force field parameters for Sn were taken from our previous work,[7] and Zr and Hf sigma values were extrapolated from the atomic radii. Bulk and interfacial ab initio MD simulations were performed for 100 ps with a 2 fs timestep in triplicate using the Vienna ab initio Simulation Package (VASP)[53,54] at 723.15 K with the projector-augmented wave (PAW)[55] method, the PBE exchange correlation functional,[56] an energy cutoff of 250 eV, and the gamma point only for the k-point grid. For interfacial systems, a 15 Å vacuum spacer was added in the *z* dimension. Following equilibration, six O_2 molecules were added to the interfacial system and the timestep was reduced to 0.5 fs and the energy cutoff was increased to 500 eV, and an additional 30 ps of AIMD simulation was performed. All analysis was carried out using VMD 1.9.3.[57,58]

Crystallographic Simulations: The crystallographic simulations were carried out by VESTA (Visualizations for Electronics and Structural Analysis) software V3.4.3.

Ferroelectricity Measurements: To investigate the ferroelectricity and electrically switchable polarization characteristics of 2D SnO-HZO, spectroscopic PFM measurements were used. The scanning probe microscopy measurements were implemented on a commercial AIST-NT SmartSPM 1000 atomic force microscope at room temperature under ambient conditions. A Pt coated silicon probe (NSC35/Pt, MikroMasch) with a tip radius of ≈30 nm was used for ferroelectric measurements. Spectroscopic PFM measurements were performed following well-established procedures after calibration of the tip's spring constant (≈8 N m^{-1}) using the thermal noise method and inverse optical lever sensitivity and considering the quality factor (Q) of the tip-sample contact resonance. To establish the veracity of the measured response, the results were compared and benchmarked against a periodically poled lithium niobate (PPLN) – a standard ferroelectric test sample. The PFM measurements were performed at an AC bias of 1 V and a frequency of ≈600 kHz over an area consisting of 40 × 20 points. The spectroscopic piezoresponse hysteresis loops were acquired at several fixed spatial locations by supplying a triangular DC waveform with a superimposed low-amplitude AC modulation. Ferroelectric *P-E* hysteresis were acquired at room temperature by the Radiant ferroelectric workstation (Precision Multiferroic II). Round Au/Cr electrodes (50/5 nm thick) with a diameter of 15 µm were deposited on SnO-HZO nanosheet using a lithography system (MLA100 Heidelberg Instruments) and an e-beam evaporator deposition system (HHV, ATS500).

Supporting Information

Supporting Information is available from the Wiley Online Library or from the author.

Acknowledgements

This work was supported by the Australian Research Council (ARC) Laureate Fellowship grant (FL180100053), the ARC Center of Excellence FLEET (CE170100039), and the ARC Industrial Hub (IH210100025). The authors also acknowledge the facilities and the scientific and technical assistance of Microscopy Australia at the Electron Microscope Unit (EMU) within the Mark Wainwright Analytical Center (MWAC) at UNSW Sydney. This research was undertaken with the assistance of supercomputing resources from the National Computational Infrastructure (NCI), which was supported by the Australian Government, under the National Computational Merit Allocation Scheme, and supported by resources provided by the Pawsey Supercomputing Research Center with funding from the Australian Government and the Government of Western Australia. P.S. acknowledges support from Flinders University's start-up grant (343.13426 – 22).

Open access publishing facilitated by The University of Sydney, as part of the Wiley - The University of Sydney agreement via the Council of Australian University Librarians.

Conflict of Interest

The authors declare no conflict of interest.

Data Availability Statement

The data that support the findings of this study are available from the corresponding author upon reasonable request.

Keywords

atomically thin, doping, HZO, liquid metal, SnO

Received: October 31, 2023
Revised: January 9, 2024
Published online: January 23, 2024

[1] C. Wang, L. You, D. Cobden, J. Wang, *Nat. Mater.* **2023**.
[2] D. Zhang, P. Schoenherr, P. Sharma, J. Seidel, *Nat. Rev. Mater.* **2023**, *8*, 25.

[3] D. D. Fong, G. B. Stephenson, S. K. Streiffer, J. A. Eastman, O. Auciello, P. H. Fuoss, C. Thompson, *Science* **2004**, *304*, 1650.
[4] S. H. Kim, I.-H. Baek, D. H. Kim, J. J. Pyeon, T.-M. Chung, S.-H. Baek, J.-S. Kim, J. H. Han, S. K. Kim, *J. Mater. Chem. C.* **2017**, *5*, 3139.
[5] S. S. Cheema, N. Shanker, L.-C. Wang, C.-H. Hsu, S.-L. Hsu, Y.-H. Liao, M. San Jose, J. Gomez, W. Chakraborty, W. Li, J.-H. Bae, S. K. Volkman, D. Kwon, Y. Rho, G. Pinelli, R. Rastogi, D. Pipitone, C. Stull, M. Cook, B. Tyrrell, V. A. Stoica, Z. Zhang, J. W. Freeland, C. J. Tassone, A. Mehta, G. Saheli, D. Thompson, D. I. Suh, W.-T. Koo, K.-J. Nam, et al., *Nature* **2022**, *604*, 65.
[6] T. Daeneke, P. Atkin, R. Orrell-Trigg, A. Zavabeti, T. Ahmed, S. Walia, M. Liu, Y. Tachibana, M. Javaid, A. D. Greentree, S. P. Russo, R. B. Kaner, K. Kalantar-Zadeh, *ACS Nano.* **2017**, *11*, 10974.
[7] M. B. Ghasemian, A. Zavabeti, M. Mousavi, B. J. Murdoch, A. J. Christofferson, N. Meftahi, J. Tang, J. Han, R. Jalili, F.-M. Allioux, M. Mayyas, Z. Chen, A. Elbourne, C. F. McConville, S. P. Russo, S. Ringer, K. Kalantar-Zadeh, *Adv. Mater.* **2021**, *33*, 2104793.
[8] N. F. Quackenbush, J. P. Allen, D. O. Scanlon, S. Sallis, J. A. Hewlett, A. S. Nandur, B. Chen, K. E. Smith, C. Weiland, D. A. Fischer, J. C. Woicik, B. E. White, G. W. Watson, L. F. J. Piper, *Chem. Mater.* **2013**, *25*, 3114.
[9] Y. Tang, C.-H. Huang, K. Nomura, *ACS Nano.* **2022**, *16*, 3280.
[10] M. B. Ghasemian, T. Daeneke, Z. Shahrbabaki, J. Yang, K. Kalantar-Zadeh, *Nanoscale* **2020**, *12*, 2875.
[11] T. S. Böscke, J. Müller, D. Bräuhaus, U. Schröder, U. Böttger, *Appl. Phys. Lett.* **2011**, *99*, 102903.
[12] J. Müller, T. S. Böscke, U. Schröder, S. Mueller, D. Bräuhaus, U. Böttger, L. Frey, T. Mikolajick, *Nano Lett.* **2012**, *12*, 4318.
[13] Y. Wei, P. Nukala, M. Salverda, S. Matzen, H. J. Zhao, J. Momand, A. S. Everhardt, G. Agnus, G. R. Blake, P. Lecoeur, B. J. Kooi, J. Íñiguez, B. Dkhil, B. Noheda, *Nat. Mater.* **2018**, *17*, 1095.
[14] J. Müller, T. S. Böscke, D. Bräuhaus, U. Schröder, U. Böttger, J. Sundqvist, P. Kücher, T. Mikolajick, L. Frey, *Appl. Phys. Lett.* **2011**, *99*, 112901.
[15] O. Ohtaka, H. Fukui, T. Kunisada, T. Fujisawa, K. Funakoshi, W. Utsumi, T. Irifune, K. Kuroda, T. Kikegawa, *J. Am. Ceram. Soc.* **2001**, *84*, 1369.
[16] M. H. Park, Y. H. Lee, H. J. Kim, Y. J. Kim, T. Moon, K. D. Kim, J. Müller, A. Kersch, U. Schroeder, T. Mikolajick, C. S. Hwang, *Adv. Mater.* **2015**, *27*, 1811.
[17] Z. Zhang, S.-L. Hsu, V. A. Stoica, H. Paik, E. Parsonnet, A. Qualls, J. Wang, L. Xie, M. Kumari, S. Das, Z. Leng, M. McBriarty, R. Proksch, A. Gruverman, D. G. Schlom, L.-Q. Chen, S. Salahuddin, L. W. Martin, R. Ramesh, *Adv. Mater.* **2021**, *33*, 2006089.
[18] Y. Lee, H. Alex Hsain, S. S. Fields, S. T. Jaszewski, M. D. Horgan, P. G. Edgington, J. F. Ihlefeld, G. N. Parsons, J. L. Jones, *Appl. Phys. Lett.* **2021**, *118*, 012903.
[19] M. H. Park, T. Schenk, C. M. Fancher, E. D. Grimley, C. Zhou, C. Richter, J. M. LeBeau, J. L. Jones, T. Mikolajick, U. Schroeder, *J. Mater. Chem. C.* **2017**, *5*, 4677.
[20] Y. Yun, P. Buragohain, M. Li, Z. Ahmadi, Y. Zhang, X. Li, H. Wang, J. Li, P. Lu, L. Tao, H. Wang, J. E. Shield, E. Y. Tsymbal, A. Gruverman, X. Xu, *Nat. Mater.* **2022**, *21*, 903.
[21] S. Shi, H. Xi, T. Cao, W. Lin, Z. Liu, J. Niu, D. Lan, C. Zhou, J. Cao, H. Su, T. Zhao, P. Yang, Y. Zhu, X. Yan, E. Y. Tsymbal, H. Tian, J. Chen, *Nat. Commun.* **2023**, *14*, 1780.
[22] X. Guo, Y. Wang, A. Elbourne, A. Mazumder, C. K. Nguyen, V. Krishnamurthi, J. Yu, P. C. Sherrell, T. Daeneke, S. Walia, Y. Li, A. Zavabeti, *Nanoscale* **2022**, *14*, 6802.
[23] A. Zavabeti, P. Aukarasereenont, H. Tuohey, N. Syed, A. Jannat, A. Elbourne, K. A. Messalea, B. Y. Zhang, B. J. Murdoch, J. G. Partridge, M. Wurdack, D. L. Creedon, J. van Embden, K. Kalantar-Zadeh, S. P. Russo, C. F. McConville, T. Daeneke, *Nat. Electron.* **2021**, *4*, 277.
[24] R. S. Datta, N. Syed, A. Zavabeti, A. Jannat, M. Mohiuddin, M. Rokunuzzaman, B. Yue Zhang, M. A. Rahman, P. Atkin, K. A. Messalea, M. B. Ghasemian, E. D. Gaspera, S. Bhattacharyya, M. S. Fuhrer, S. P. Russo, C. F. McConville, D. Esrafilzadeh, K. Kalantar-Zadeh, T. Daeneke, *Nat. Electron.* **2020**, *3*, 51.
[25] M. B. Ghasemian, M. Mayyas, S. A. Idrus-Saidi, M. A. Jamal, J. Yang, S. S. Mofarah, E. Adabifiroozjaei, J. Tang, N. Syed, A. P. O'Mullane, T. Daeneke, K. Kalantar-Zadeh, *Adv. Funct. Mater.* **2019**, *29*, 1901649.
[26] M. Hyuk Park, H. Joon Kim, Y. Jin Kim, W. Lee, H. Kyeom Kim, C. Seong Hwang, *Appl. Phys. Lett.* **2013**, *102*, 112914.
[27] L. Tang, H. Maruyama, T. Han, J. C. Nino, Y. Chen, D. Zhang, *Appl. Surf. Sci.* **2020**, *515*, 146015.
[28] A. Goff, P. Aukarasereenont, C. K. Nguyen, R. Grant, N. Syed, A. Zavabeti, A. Elbourne, T. Daeneke, *Dalton Trans.* **2021**, *50*, 7513.
[29] A. Zavabeti, J. Z. Ou, B. J. Carey, N. Syed, R. Orrell-Trigg, E. L. H. Mayes, C. Xu, O. Kavehei, A. P. O'Mullane, R. B. Kaner, K. Kalantar-zadeh, T. Daeneke, *Science* **2017**, *358*, 332.
[30] M. B. Ghasemian, A. Zavabeti, R. Abbasi, P. V. Kumar, N. Syed, Y. Yao, J. Tang, Y. Wang, A. Elbourne, J. Han, M. Mousavi, T. Daeneke, K. Kalantar-Zadeh, *J. Mater. Chem. A.* **2020**, *8*, 19434.
[31] Y. Park, V. Choong, Y. Gao, B. R. Hsieh, C. W. Tang, *Appl. Phys. Lett.* **1996**, *68*, 2699.
[32] W. Hamouda, A. Pancotti, C. Lubin, L. Tortech, C. Richter, T. Mikolajick, U. Schroeder, N. Barrett, *J. Appl. Phys.* **2020**, *127*, 064105.
[33] M. Thirumoorthi, J. T. J. Prakash, *Superlattices Microstruct.* **2016**, *89*, 378.
[34] T. S. Moss, *Proc. Phys. Soc. B.* **1954**, *67*, 775.
[35] B. Liu, J. Ma, H. Zhao, Y. Chen, H. Yang, *Appl. Phys. A.* **2012**, *107*, 437.
[36] C. Ton-That, L. Weston, M. R. Phillips, *Phys. Rev. B.* **2012**, *86*, 115205.
[37] P. Sharma, F.-X. Xiang, D.-F. Shao, D. Zhang, E. Y. Tsymbal, A. R. Hamilton, J. Seidel, *Sci. Adv.*, *5*, eaax5080.
[38] S. Starschich, U. Böttger, *J. Appl. Phys.* **2018**, *123*, 044101.
[39] I. Stolichnov, M. Cavalieri, E. Colla, T. Schenk, T. Mittmann, T. Mikolajick, U. Schroeder, A. M. Ionescu, *ACS Appl. Mater. Interfaces* **2018**, *10*, 30514.
[40] L. Collins, U. Celano, *arXiv preprint* arXiv:2004.12903 **2020**.
[41] M. Falkowski, A. Kersch, *ACS Appl. Mater. Interfaces* **2020**, *12*, 32915.
[42] H. A. Hsain, P. Sharma, H. Yu, J. L. Jones, F. So, J. Seidel, *Appl. Phys. Lett.* **2018**, *113*, 022905.
[43] B. Prasad, V. Thakare, A. Kalitsov, Z. Zhang, B. Terris, R. Ramesh, *Adv. Electron. Mater.* **2021**, *7*, 2001074.
[44] H. Y. Yoong, H. Wu, J. Zhao, H. Wang, R. Guo, J. Xiao, B. Zhang, P. Yang, S. J. Pennycook, N. Deng, X. Yan, J. Chen, *Adv. Funct. Mater.* **2018**, *28*, 1806037.
[45] P. Sharma, S. Ryu, Z. Viskadourakis, T. R. Paudel, H. Lee, C. Panagopoulos, E. Y. Tsymbal, C.-B. Eom, A. Gruverman, *Adv. Funct. Mater.* **2015**, *25*, 6538.
[46] S. S. Cheema, D. Kwon, N. Shanker, R. dos Reis, S.-L. Hsu, J. Xiao, H. Zhang, R. Wagner, A. Datar, M. R. McCarter, C. R. Serrao, A. K. Yadav, G. Karbasian, C.-H. Hsu, A. J. Tan, L.-C. Wang, V. Thakare, X. Zhang, A. Mehta, E. Karapetrova, R. V. Chopdekar, P. Shafer, E. Arenholz, C. Hu, R. Proksch, R. Ramesh, J. Ciston, S. Salahuddin, *Nature* **2020**, *580*, 478.
[47] F. Yan, G. Xing, R. Wang, L. Li, *Sci. Rep.* **2015**, *5*, 9128.
[48] Y. Chen, L. Wang, L. Liu, L. Tang, X. Yuan, H. Chen, K. Zhou, D. Zhang, *J. Mater. Sci.* **2021**, *56*, 6064.
[49] R. J. Zeches, M. D. Rossell, J. X. Zhang, A. J. Hatt, Q. He, C. H. Yang, A. Kumar, C. H. Wang, A. Melville, C. Adamo, G. Sheng, Y. H. Chu, J. F. Ihlefeld, R. Erni, C. Ederer, V. Gopalan, L. Q. Chen, D. G. Schlom, N. A. Spaldin, L. W. Martin, R. Ramesh, *Science* **2009**, *326*, 977.
[50] N. Cabrera, N. F. Mott, *Rep. Prog. Phys.* **1949**, *12*, 163.
[51] B. D. Viezbicke, S. Patel, B. E. Davis, D. P. Birnie Iii, *Phys. Status Solidi B.* **2015**, *252*, 1700.
[52] S. Plimpton, *J. Comput. Phys.* **1995**, *117*, 1.

[53] G. Kresse, J. Furthmüller, *Phys. Rev. B.* **1996**, *54*, 11169.
[54] G. Kresse, D. Joubert, *Phys. Rev. B.* **1999**, *59*, 1758.
[55] P. E. Blöchl, *Phys. Rev. B.* **1994**, *50*, 17953.
[56] J. P. Perdew, K. Burke, M. Ernzerhof, *Phys. Rev. Lett.* **1996**, *77*, 3865.
[57] W. Humphrey, A. Dalke, K. Schulten, *J. Mol. Graph.* **1996**, *14*, 33.
[58] T. Giorgino, *J. Open Source Softw.* **2019**, *4*, 1698.